ISABE-2015-20021

CFD Based Comparison of the Aerodynamics within S-Duct Inlet Configurations at Sub- and Full-Scale Engine Test Facilities

Sebastian Brehm, Rudolf P. M. Rademakers, Stefan Bindl, Reinhard Niehuis
Universität der Bundeswehr München
Institute of Jet Propulsion
sebastian.brehm@unibw.de

Abstract

In future civil air transportation concepts and modern military air systems, the integration of the propulsion system into the airframe usually leads to highly contoured intake geometries. These designs can cause significant distortions in the air flow delivered to the compressor of the jet engine. Therefore, investigations on the interaction phenomena between the aerodynamics within the inlet duct and the response of the compressor system are inevitable.

In the near future, the Institute of Jet Propulsion at the University of the German Federal Armed Forces Munich will conduct experimental investigations with highly curved intake ducts attached to two different jet engines within a jet Engine Test Facility (ETF). Besides this, a Scaled jet Engine Test Facility (SETF) is operated which allows experimental investigations of duct aerodynamics with significantly reduced effort in terms of monetary expense and time.

Within this paper, the qualitative and quantitative transferability of the inner duct aerodynamics between both facilities, the ETF and the SETF, is investigated. For this purpose, validated CFD simulations of two different duct geometries within both facilities are utilized. In order to enable similarity in terms of the intake duct inflow Mach number in the ETF and the SETF, a correlation procedure is established and validated. Furthermore, the strength of total pressure and swirl distortions quantified by dedicated parameters is compared. Differences are discussed with regard to the different Reynolds number levels present in the full scale and the sub-scale engine test facility.

Nomenclature

Symbols

A	$[m^2]$	cross-sectional area
c	$[m/s]$	velocity
$DC60$	$[-]$	60° Distortion Coefficient
$\dot{m}$	$[^{kg}/_{s}]$	mass flow rate
Ma_{is}	$[-]$	isentropic Mach number
n_{rel}	[%]	relative spool speed
p	$[Pa]$	pressure
r	$[m]$	radius
$SC60$	$[-]$	60° Swirl Coefficient
T	$[K]$	temperature
x	$[m]$	axial position
κ	$[-]$	ratio of specific heats
Π	$[-]$	pressure ratio

Abbreviations

AIP	Aerodynamic Interface Plane
CCOP	Correspond. Central Operating Point
CFD	Computational Fluid Dynamics
CLOP	Correspond. Lower Operating Point
CUOP	Correspond. Upper Operating Point
ETF	Engine Test Facility
EXP	Experimental
MPS	Maximum Power Setting
SETF	Scaled Engine Test Facility

Subscripts

max	maximum
min	minimum
ref	reference
red	reduced
t	total
60	60° segment
Φ	circumferential

1. Introduction

The improvement of the so-called "stealth capabilities" became a key issue in the design of modern tactical aircraft (Hamstra & McCallum (2010)). One measure to reduce the radar cross-section is to shield the low pressure compressor of the jet engine from direct sight as it is extremely reflective. This can be achieved by the use of highly curved air intake ducts which allow full engine integration into the fuselage.

The redirections of the flow within the intake to ensure full engine obscuration at short axial dimensions usually lead to partly significant distortions in the flow field upstream of the low pressure compressor. Both the likely occurring total pressure and swirl non-uniformities evoke undesirable effects concerning the engine. These are for example:

- Reduced surge margin which can cause aerodynamic instabilities within the compressor (Bissinger & Breuer (2010))
- Decreased thrust (Bissinger & Breuer (2010))
- Increased fan noise and high-cycle fatigue (Sobester (2007))

These problems are also present in future civil air transportation concepts such as the "Blended-Wing-Body" (Berrier & Allan (2004)), where a full integration of the engine into the fuselage is a promising approach to reduce the aircraft's overall drag. Therefore, extensive research is carried out regarding the aerodynamic conditions within highly bended intakes. In many publications in this area, CFD is utilized to investigate different aspects such as the influence of varying duct geometries (e.g. Kächele et al. (2015), Kächele et al. (2015)) or inflow conditions (e.g. Berrier & Allan (2004), Brehm et al. (2014)).

In order to take into account the mutual interaction between flow distortions and response of the compression system, an "integrated approach" is recommended by e.g. Bindl et al. (2015), Cousins (2004), or Davis et al. (2002). The Institute of Jet Propulsion at the University of the German Federal Armed Forces Munich operates an enclosed Engine Test Facility (ETF) in which several modern jet engines are in service (cf. Bindl et al. (2009)). In the near future, two different jet engines are going to be operated with highly curved intake geometries within the ETF. Such an approach enables investigations on both the intake's inner aerodynamics as well as the response of the low pressure compressors within a single setup.

Besides this, a sub-scale model of the ETF, called Scaled Engine Test Facility (SETF) has been set up. Using the SETF for experimental investigations of the aerodynamics within contoured ducts (cf. Rademakers et al. (2013)) allows significant reductions in cost and time necessary for jet engine operation and especially for manufacturing the intakes.

To maximize synergy effects and to take advantage of the benefits of both facilities, the question on transferability of results between the ETF and the SETF arises. Within this context, especially two topics have to be considered:

1. A "correlation procedure" is required to ensure corresponding engine tests in both facilities satisfy Mach number similarity.
2. Different Reynolds number levels are present due to the significantly different dimensions of the facilities and therefore also of the ducts.

Within this paper, such a correlation procedure is established. It is validated by means of CFD simulations which are conducted for two different intake geometries in both facilities. Furthermore, the CFD results are used to quantify the effects of different Reynolds number levels on the distortions generated by the highly curved ducts.

2. Engine test facilities and intake geometries

2.1 Engine Test Facility (ETF)

An enclosed ground jet Engine Test Facility (ETF) is in service since the late 1970's at the Institute of Jet Propulsion at the University of the German Federal Armed Forces Munich. It was designed for testing of military turbojet and turbofan engines but also of their turbomachinery components for research and educational purposes.

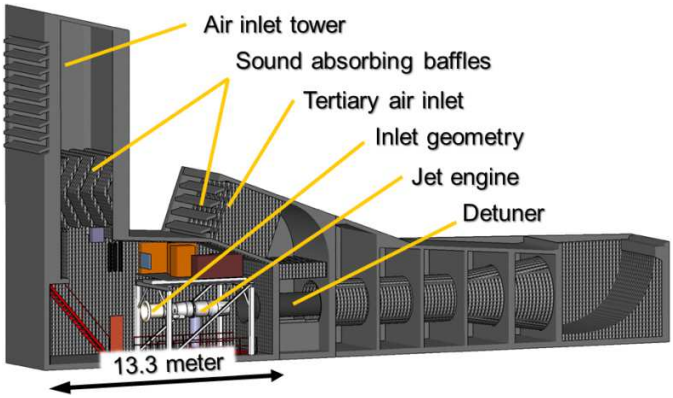

Figure 1. Engine Test Facility (ETF)

The ETF features an unconventional design concerning the air inflow in comparison to most of the test beds operated for industrial testing. Figure 1 depicts the ETF with its main components. Primary and secondary air is drawn into the test cell tangentially to the sound absorbing cascades installed in an air inlet tower. Hence, the air aspirated by the jet engines (primary air) is deflected downward which is resulting in non-uniform inflow conditions to the intake ducts. Furthermore, the flow conditions upstream of the intake ducts are influenced significantly by the secondary air mass flow. This additional air mass flow is entrained due to the ejector effect establishing between the hot and fast exhaust gas plume and the detuner (cf. fig. 1). The ejector effect is also entraining tertiary air further downstream for cooling and noise reduction before the entire air flow is discharged into atmosphere (see also fig. 1).

Currently, four military jet engines, including the More electric experimental Jet Engine Test vehicle MexJET based on the *EJ200* engine and a *Larzac 04* twin-spool turbofan, can be operated at the ETF (see Bindl et al. (2009) and Bindl et al. (2013) for details). The latter is highly instrumented with arrays of *Kulite*-pressure sensors and stator blade total pressure taps for example. The presented paper is focussing on this engine, since it is predestined to study the interaction phenomena between engine inlet flow distortions and low pressure compressor aerodynamics.

2.2 Scaled Engine Test Facility (SETF)

The Institute of Jet Propulsion has also set up a subscale model of the original ETF at a scale of 1:7. This Scaled Engine Test Facility (SETF) allows extremely cost and time efficient experimental investigations. It features all relevant components of the ETF as depicted in fig. 2.

A small commercial single spool gas turbine (*G-BOOSTER 160* from *Graupner*) is emulating the full-scale jet engine in the ETF (in this case the *Larzac 04* as stated previously). The SETF can be operated in two different configurations: The basic and the test cell configuration (cf. fig. 2). In basic configuration, the air is entering the rectangular test cell in axial direction. This case is used for e.g. basic research on the ejector effect. However, since this paper is comparing the aerodynamics within different intake geometries operated in the ETF and the SETF, the test cell configuration will be utilized instead. Here, the air is guided into the test cell by the applied sound absorbing baffles analog to the ETF.

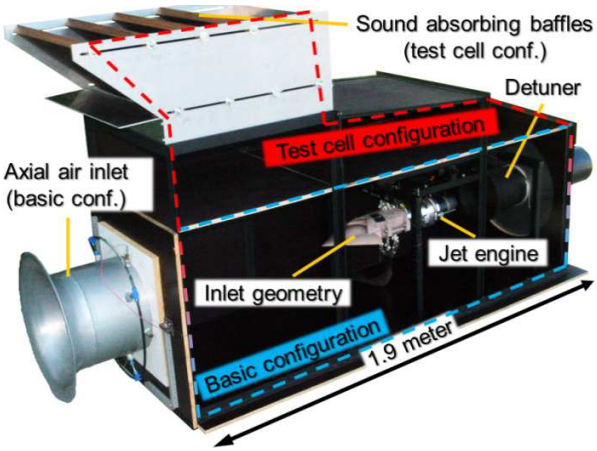

Figure 2. Scaled Engine Test Facility (SETF)

The total pressure characteristics within the AIP are measured by means of a total pressure rake, constituted of 6 arms with 5 total pressure probes per arm (cf. fig. 6). Upstream of the measurement rake, arbitrary duct geometries can quickly be attached to the engine.

It is referred to the work of Bindl et al. (2012) and Rademakers et al. (2013) for details concerning further measurement equipment, data acquisition, and the small gas turbine.

2.3 Duct geometry 1

Duct geometry 1 is a generic single s-shaped intake geometry used in several investigations in the past (e.g. by Vuillerme et al. (2005)).

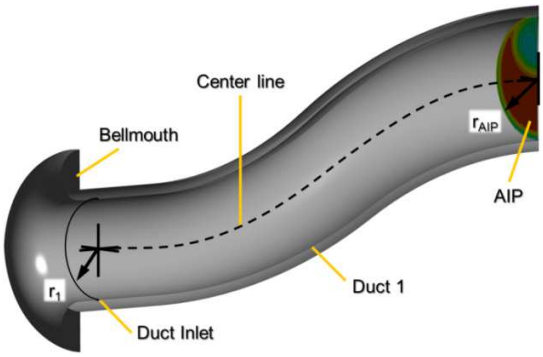

Figure 3. Duct geometry 1 (generic inlet duct)

The centerline is defined by two tangential arcs subtending an angle of 30° each and all cross-sections are of circular shape. Their radii increase from the inlet (r_1) to the AIP (r_{AIP}) of the particular engine in stream-wise direction with a factor of r_{AIP}/r_1=1.23 (diffusing characteristic). A bellmouth is attached upstream to ensure smooth inflow. The duct geometry with bellmouth and a characteristic flow distortion in the AIP is depicted in fig. 3.

2.4 Duct geometry 2

Duct geometry 2 is a generic duct and was originally designed by Airbus Defense and Space. A section throughout the stream-wise symmetry plane is shown in fig. 4. It features characteristics which are specific for diverter-less inlet geometries of modern unmanned aerial systems: A so-called "bump" is positioned upstream of the inlet plane to prevent low energetic boundary layer fluid formed by the fuselage forebody from entering the duct. The cross-sections of the duct are changing both in shape (wedge-shaped to circular as depicted in fig. 4) and area (increasing) towards the AIP. A double s-shaped centerline is reducing direct sight onto the jet engine's compressor.

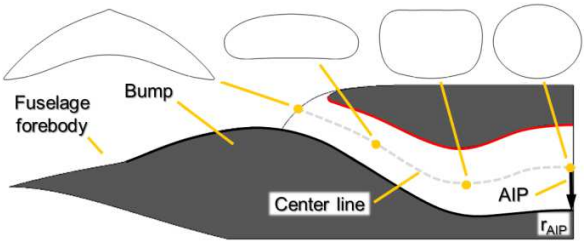

Figure 4. Duct geometry 2

A sub-scale model of duct 2 was manufactured in-house in less than one week for experimental investigations in the SETF.

It features in total 71 wall pressure taps along the symmetry plane: 44 thereof at the bottom (locations indicated in black in fig. 4) and 27 at the upper side (locations indicated in red in fig. 4).

3. CFD setups

3.1 Computational grids

In both setups, the computational domain is ranging from atmosphere upstream of the air inlet tower or of the sound absorbing cascades, respectively, to atmosphere downstream of the detuner outlets (cf. fig. 1 and fig. 2). Both the ETF domain as well as the SETF domain are split up in several mesh modules. These contain specific components of the facilities such as the engine or the intake geometry. The mesh of each modul is generated separately in *ANSYS ICEM CFD 12.1* and they are connected via grid interfaces. This approach enables rapid interchangeability of certain modules like engines or intakes without the need to remesh the entire domain.

Most of the meshes are of hexahedral cells generated with a blocking based approach. For simulation of intake duct 2 within the SETF, tetrahedral cells with prismatic wall resolution are used. The overall node numbers resulting from mesh-independency studies are shown in tab. 1 for both inlet ducts in both facilities.

Table 1. Number of overall mesh nodes

	Duct 1	Duct 2
ETF	11,371,057	13,645,770
SETF	13,362,536	10,343,899

3.2 Boundary conditions

In order to reduce the computational effort, a symmetry boundary condition is applied in longitudinal direction for both facilities. All walls are modelled as no-slip (hydraulically smooth) and adiabatic. Atmospheric conditions upstream and downstream of the facilities are represented by boundary conditions based on total pressure/total temperature and static pressure, respectively. The inlets of the jet engine compressors are modelled by mass-flow based boundary conditions. The same applies for the core nozzles in general and also for the bypass nozzle in case of the *Larzac 04*. In addition, total exhaust gas temperatures are specified at the respective engine nozzles. For the *Larzac 04*, also the bypass total temperature is set. Details on the determination of the boundary conditions are also given in chapter *Correlation Procedure*.

3.3 Solver and numerical settings

All calculations are carried out as fully turbulent RANS simulations in *ANSYS CFX 14.0*.

In all cases, the two-equation shear stress transport turbulence model with activated curvature correction is applied. This setting has shown the best performance with regard to the inner aerodynamics of duct 1 as shown by Brehm et al. (2014).

The conducted mesh-independency studies showed that treatment of the boundary layers with wall functions is sufficient for the investigations carried out within this paper.

4. Description Parameters

In order to characterize the internal flow within the ducts and also for comparison of different aerodynamic operating points, pressure values are non-dimensionalized by means of the isentropic Mach number (defined according to eq. 1).

$$Ma_{is} = \sqrt{\frac{2}{\kappa-1} \cdot \left[\left(\frac{p_{t,ref}}{p} \right)^{\frac{\kappa-1}{\kappa}} - 1 \right]} \qquad (1)$$

Dimensionless total pressure values are expressed with Π_t (eq. 2).

$$\Pi_t = \frac{p_t}{p_{t,ref}} \qquad (2)$$

Two well established distortion parameters are used here in order to describe the swirl and total pressure distortion patterns generated by the intakes under investigation. Both are evaluated with a "segment-based" approach. The so-called $SC60$ parameter is defined according to eq. 3 and used to quantify the strength of swirl distortions (cf. Schmid et al. (2000)): An arc-segment subtending 60° is spanned in circumferential direction within the AIP. The absolute maximum tangential velocity in circumferential direction within this segment $\left|\vec{c}_{\Phi,\max,60}\right|$ is then normalized with the average velocity over the entire AIP $\overline{|\vec{c}_{\mathrm{AIP}}|}$. A similar concept is used to formulate the $DC60$ parameter for description of total pressure non-uniformities. Equation 4 shows the definition of $DC60$. Since the 60° segment can be positioned arbitrarily in circumferential direction, determination of circumferential $DC60$ and $SC60$ characteristics is enabled, too.

$$SC60 = \frac{\left|\vec{c}_{\Phi,\max,60}\right|}{\overline{|\vec{c}_{\mathrm{AIP}}|}} \qquad (3)$$

$$DC60 = \frac{\overline{p_{t,AIP}} - \overline{p_{t,60}}}{\overline{p_{t,AIP}} - \overline{p_{AIP}}} \qquad (4)$$

5. CFD validation

5.1 Engine test facilities (ETF and SETF)

The aerodynamic conditions within the test cells of the ETF and the SETF can be predicted fairly well by the established CFD simulation setups (cf. Bindl et al. (2009), Muth et al. (2012)). This applies not only in terms of quantitative parameters like the amount of secondary air entrained due to the ejector effect or the static pressure levels within the test cells. Furthermore, Bindl et al. (2009) and Bindl et al. (2012) have shown that the macro flow features in both engine test facilities caused by the unconventional test cell designs are basically identical.

5.2 Duct geometry 1

The CFD predictions of the aerodynamic conditions within duct geometry 1 have already been validated in detail by Brehm et al. (2014) utilizing extensive experimental measurements published by Wellborn & Okiishi (1993). It was found that the onset position of the separation is predicted correctly, but the extension of the separation region perpendicular to stream-wise direction seems to be less extended in CFD compared to the experiments. It is referred to Brehm et al. (2014) for details.

Concerning the quantitative prediction, it can be stated that undistorted portions of the flow show total pressure levels which are too high compared to experiments. The total pressure losses within portions affected by the separation located upstream are usually over-predicted on the other hand. This leads to partly higher values of the $DC60$ parameter in CFD (Vuillerme et al. (2005), Brehm et al. (2014)). Although, these deviations are expected to be independent of the Reynolds number level present and therefore, comparability of results gathered with CFD simulations of both facilities can be assumed for the presented investigations. Furthermore, the over-prediction of total pressure distortion parameters by CFD is favorable compared to an under-estimation with regard to a safe engine operation in the test facilities since in reality, total pressure distortions are expected to be lower.

5.3 Duct geometry 2

To validate the CFD predictions for duct geometry 2, experimental measurements obtained within the subscale duct manufactured in-house and operated at the SETF are utilized.

Test cell configuration of the SETF (fig. 2) is applied and the engine has been operated at maximum power setting (MPS).

The center part of fig. 5 shows a Mach number contour plot in the duct symmetry plane where a large recirculation structure detaching from the upper intake lip is obvious. Furthermore, fig. 5 depicts the wall pressure distributions in terms of the isentropic Mach number, both experimental and CFD, for the upper (red) and the lower symmetry plane surface (black).

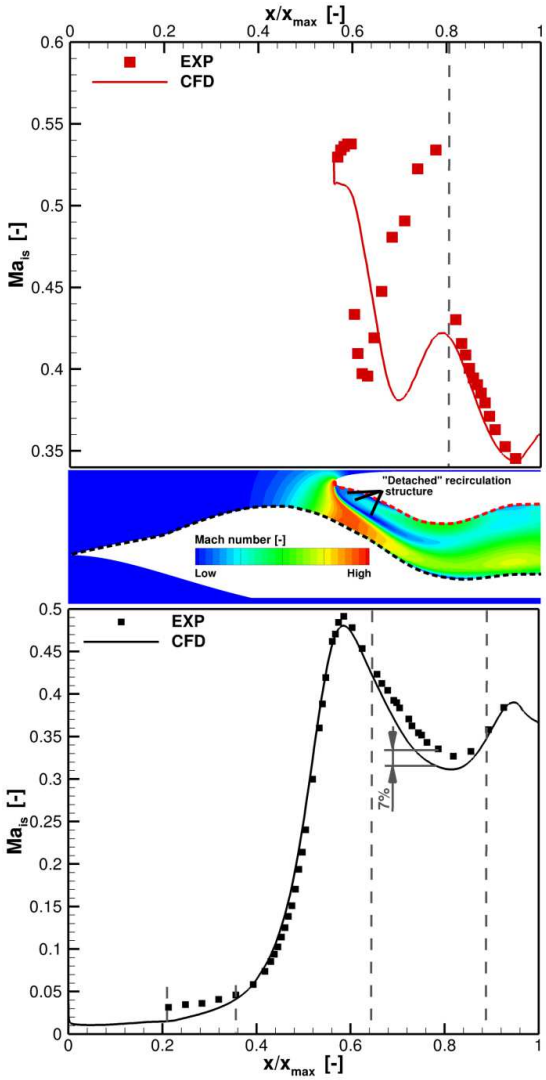

Figure 5. Isentropic Mach number on the symmetry plane surface of duct geometry 2 at MPS in the SETF (test cell configuration)

As can be seen, CFD predicts the pressure distribution on the bottom side of the symmetry plane (black line) quite well. Besides parts of the fuselage forebody, only the deceleration between $x/x_{max} \approx 0.64$ and $x/x_{max} \approx 0.88$ downstream of the suction peak is under-estimated (maximum deviation about 7% of Ma_{is}). A similar relationship between numerical and experimental results has also been reported by Brehm et al. (2014): The extension of the recirculation region perpendicular to the duct surface seems to be predicted too small. This in turn reduces the blockage impact of the backflow and the acceleration of the remaining duct flow is less distinct in CFD due to continuity reasons.

However, the wall pressure distribution on the upper side of the duct (red line) shows a reliable quantitative prediction only downstream of $x/x_{max} \approx 0.8$. The upstream region is directly influenced by the highly three dimensional recirculation structure around the upper intake lip. This area is most likely dominated by highly unsteady flow effects which are determined only qualitatively correct by the RANS-approach. This recirculation around the lip is also responsible for the total pressure distortion present in the AIP. Figure 6 shows an exemplary comparison of the vertical total pressure profiles measured and computed throughout the AIP.

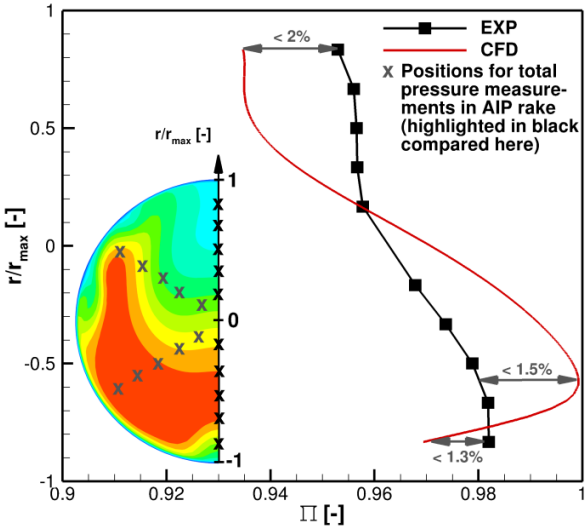

Figure 6. Vertical total pressure profile within the AIP of duct 2 at MPS in the SETF

The trend is captured well by CFD, but both local extrema of the total pressure profile are more distinct in the CFD result. The fact that similar relationships were discovered in previously conducted CFD investigations (e.g. Vuillerme et al. (2005) or Brehm et al. (2014)), too and also the consequences for the CFD investigations presented within this paper have already been discussed above.

6. Correlation procedure

In order to enable a reasonable comparison of the aerodynamics within ducts operated in the ETF and the SETF, certain fluid mechanical similarities have to be considered. Geometrical similarity of the ducts is assured as they are scaled to the required AIP diameters.

The minor differences regarding the test cell designs (e.g. complete air inlet tower in the ETF compared to sound absorbing baffles only in the SETF) can affect the aerodynamics within the test cell and in turn also the inflow conditions of the ducts. These differences are addressed as described below. Furthermore, also Mach number similarity has to be assured. For this purpose, a correlation procedure has been established. It is based on the reduced duct mass flow rate $\dot{m}_{red}$, which is defined according to eq. 5:

$$\dot{m}_{red}(n_{rel}) = \frac{\dot{m}_{intake}(n_{rel})\cdot\sqrt{T_t}}{p_t(n_{rel})\cdot A_{AIP}} \qquad (5)$$

The main steps of the correlation procedure are described in the following:

1. Calculation of the reduced mass flow rate parameter: $\dot{m}_{red}$ is determined as function of the relative (low pressure) spool speed n_{rel} (thus $\dot{m}_{red} = f(n_{rel})$) for the jet engines operated in both facilities: A_{AIP} is fixed for each engine and $\dot{m}_{intake} = f(n_{rel})$ is known from experiments and the engine performance maps. The total temperature is constant since the inflow to the ducts can be considered as adiabatic. The total pressure on the other hand depends on the spool speed $f(n_{rel})$: Total pressure losses are in general increasing with higher air flow velocities. The velocity level itself is set by the amount of the total air mass flow convected through the facilities. The total air mass flow is the sum of the inlet mass flow rate $\dot{m}_{intake}$ and the secondary mass flow drawn into the facilities due to the ejector effect. However, the amount of secondary mass flow in turn is also dependent on n_{rel} due to varying combinations of exhaust gas temperatures and engine mass flow rates directly affecting the strength of the ejector effect (e.g. Bindl et al. (2012), Muth et al. (2012)).

2. Identification of the range which allows engine operation with Mach number similarity regarding the intake inflow conditions: Each engine operating point is directly linked to a certain reduced mass flow rate (and therefore also to a certain intake duct inflow Mach number). This is due to the specific engine mass flow rates of the respective jet engine in combination with the characteristic duct dimensions in both facilities. Figure 7 shows a qualitative depiction for the entire engine operation range from idle to maximum power setting (MPS) for the small jet engine *G-BOOSTER 160* (SETF, upper part of fig. 7 indicated in black) and the *Larzac 04* (ETF, lower part of fig. 7 indicated in blue).

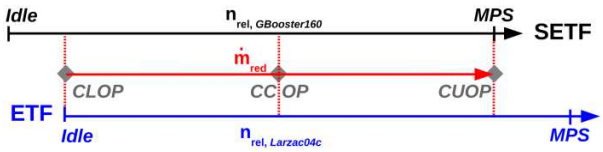

Figure 7. Definition of corresponding engine operating points

Since similarity in terms of the inflow Mach number is required for a reasonable comparison, certain operating points exist for both jet engines which share equivalent inflow Mach numbers/reduced mass flow rates respectively. This range is called "corresponding operation range" and it is indicated in red in fig. 7. The lower limit is called "Corresponding Lower Operating Point" (CLOP) and is defined by idle engine operation of the *Larzac 04*. This is the lowest $\dot{m}_{red}$ possible when operating the *Larzac 04*. Smaller values for the reduced mass flow rate parameter are only possible with the *G-BOOSTER 160* (cf. range in black left of CLOP up to idle setting). Although, these $\dot{m}_{red}$ are not sensible for comparison since they cannot be reached at the ETF. The upper limit is named "Corresponding Upper Operating Point" (CUOP) which is defined by MPS of the *G-BOOSTER 160*. A third operation point, approximately half way between CLOP and CUOP named "Corresponding Center Operating Point" (CCOP), is chosen in addition.

3. Determination of the required boundary conditions for the CFD simulations: In order to set up the corresponding engine operating points of the SETF and the ETF, the boundary conditions representing the jet engines in both CFD setups have to be set individually. The required engine intake mass flow $\dot{m}_{intake}$ is derived directly from the reduced mass flow rate $\dot{m}_{red}$ known for each corresponding operating points (in this case CLOP, CCOP, and CUOP). A correction factor is applied to consider the mentioned implicit dependency of the total pressure loss (affecting p_t) and the engine operation point. This correction factor is also taking into account the slightly different ejector effect characteristics of both facilities. As described above, these influence the duct inflow conditions which in turn should be as similar as possible. The required exhaust gas temperatures (as well as bypass temperature and bypass ratio in case of the *Larzac 04*) are available as interpolated functions of the relative (low pressure) spool speeds in a database. Thus, the established correlation procedure provides the numerical values for all boundary conditions representing the engines in the CFD simulations to enable Mach number similarity of the intake duct's inflow conditions at the corresponding engine operating points. The entire correlation procedure is implemented as *Python*-script for ease of use.

Reynolds number similarity could be enforced in CFD by altering fluid properties or pressure levels. But this would require non-acceptable effort in the experimental setups on the other hand. Since the presented investigation is to evaluate the transferability of results obtained by experiments at the SETF to a potential full scale setup in the ETF, the existing differences in the Reynolds number levels are taken into account by the CFD setup and will be quantified subsequently.

7. Results and discussion

The wall pressure distributions in the symmetry plane of both intake ducts are compared in terms of the isentropic Mach numbers resulting from the CFD simulations in both engine test facilities. This allows an assessment of the proposed correlation procedure. In general, the Ma_{is}-distributions are very similar except for those regions where flow separations are present (duct 1). Most likely this is due to the lower Reynolds number level. Deviations also occur because of installation reasons (duct 2). Therefore, the established correlation procedure can be regarded as validated. Specific aerodynamic phenomena in both ducts and a comparison of the distortion patterns developing within the AIP are discussed in more detail in the following.

7.1 Duct geometry 1

A "well established" separation region is present at the upper side of the duct downstream of $x/x_{max} \approx 0.5$ (cf. center section of fig. 8). It is more distinct in the SETF as can be seen by the more pronounced Ma_{is}-plateaus at top section of fig. 8 (dashed red lines). The reason for the intensified separation is the Reynolds number level which is lower by factor 6.5 within the SETF. This has two direct impacts: First, higher distortion intensities within the AIP are present for SETF operation as quantified later on. Secondly, the relative growth of the separation bubble leads to an increased relative blockage of the duct's aerodynamic cross-sectional area in the SETF. Thus, the remaining flow within the undistorted part of the respective cross-sections is accelerated further compared to ETF operation. This also results in higher Ma_{is}-levels on the lower side of the duct downstream of $x/x_{max} \approx 0.65$ (dashed black lines).

7.2 Duct geometry 2

In this case, extrema of the Ma_{is}-distributions, representing local minima or maxima of the flow velocities, are more pronounced in the SETF both on the upper and lower side of the intake's symmetry planes (compare dashed lines in the upper and lower sections of fig. 9). Besides this, upstream of about $x/x_{max} \approx 0.45$, differences are apparent for the lower wall. These deviations can be explained with a different axial position of the installed ducts due to the thrust frame constructions and measurement equipment in the SETF.

In this region, duct 2 is slightly more exposed to the inclined flow originating from the sound absorbing baffles (cf. Bindl et al. (2013)). This has to be considered if the ducts investigated are prone to the inflow conditions influenced by the boundary layer development over a possibly existing fuselage forebody.

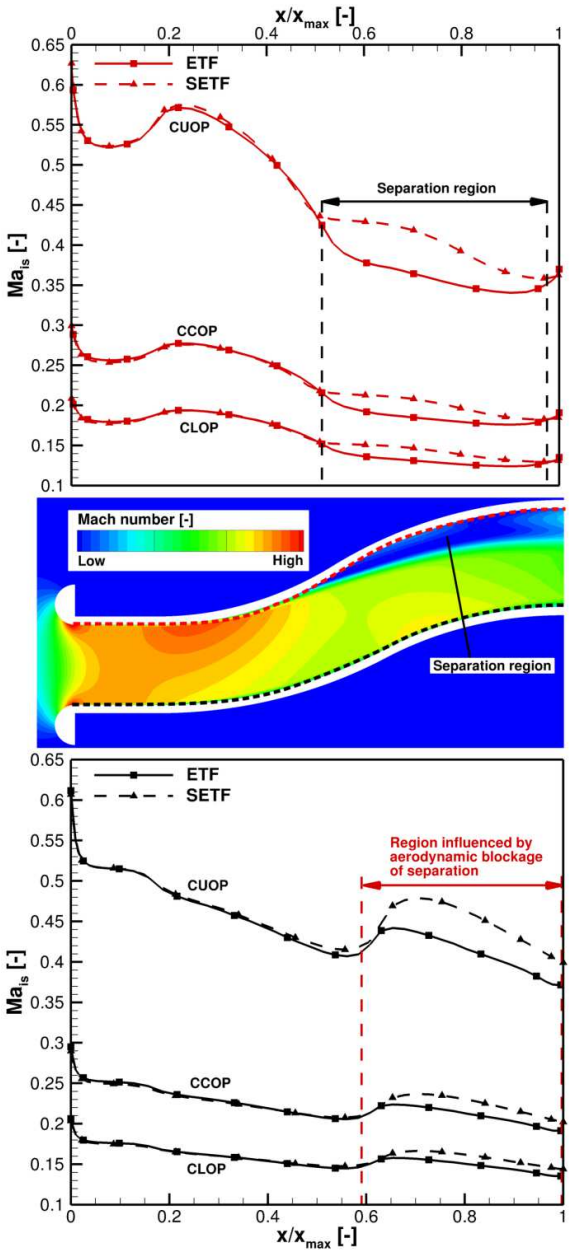

Figure 8. Isentropic Mach numbers on the symmetry plane surface of duct geometry 1 for three corresponding engine operating points

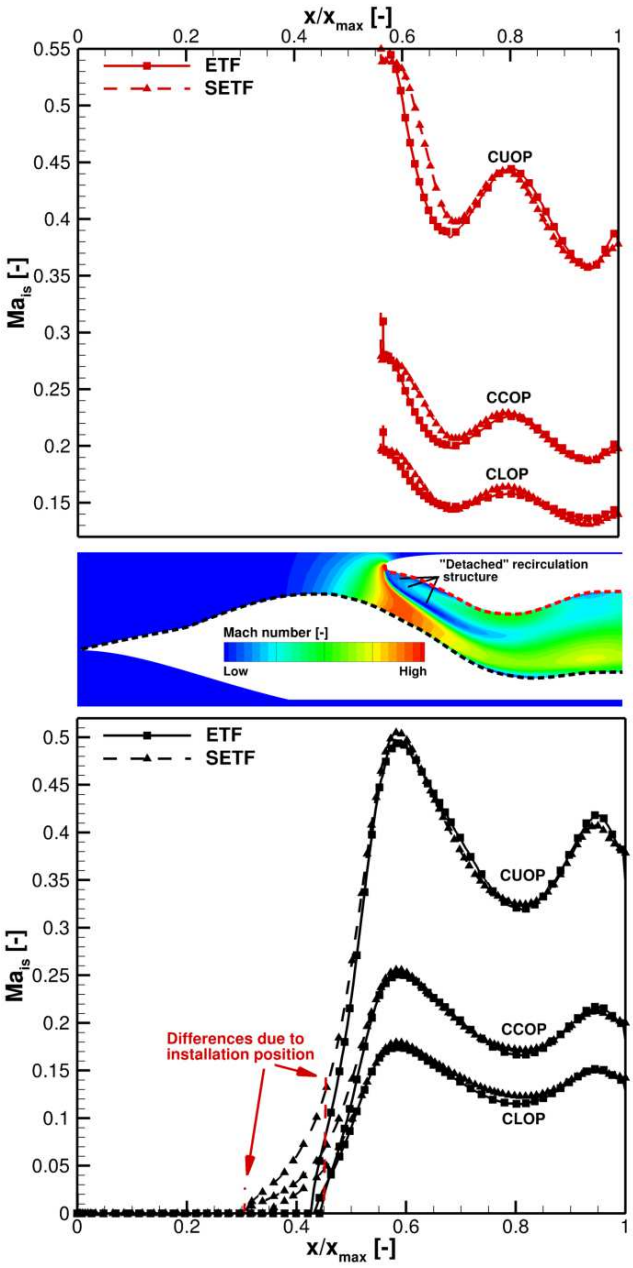

Figure 9. Isentropic Mach numbers on the symmetry plane surface of duct geometry 2 for three corresponding engine operating points

7.3 Distortions within the AIP

An investigation of the strength of total pressure and swirl distortion patterns generated by the ducts allows a comparison of the two basically different intake geometries. Furthermore, also the impact of the different Reynolds number levels present in the ETF and the SETF can be assessed. In fig. 10 and fig. 11, the maxima of the $DC60$ and the $SC60$ parameter, respectively, are depicted over the reduced engine mass flow rate $\dot{m}_{red}$ for both duct geometries in both facilities.

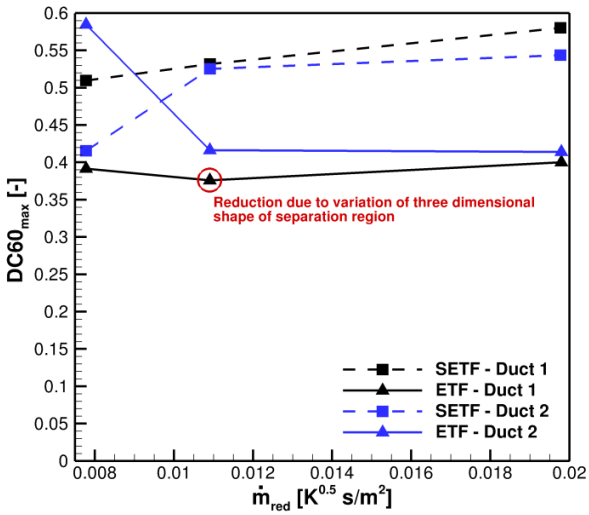

Figure 10. Total pressure distortions

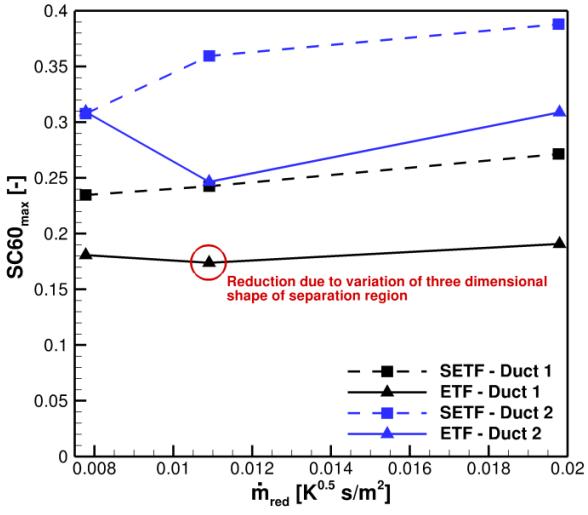

Figure 11. Swirl distortions

In general, the total pressure and swirl non-uniformities are more distinct if duct 1 (dashed black lines) is operated in the SETF. This behavior was expected due to the lower Reynolds number level (about factor of 6.5) and thus an intensified separation region in case of the SETF. Thereby, the offset is about 40% for the $DC60_{max}$ and about 30%-40% for the $SC60_{max}$. The differences rise towards increased engine mass flow rates in all cases. This means that experimental investigations performed in the SETF are more conservative in terms of a safe engine operation in the ETF with a geometrical similar duct geometry where the distortion in the AIP is caused by a well established separation region (duct 1 in this case).

It can be seen for the simulations of duct 1 within the ETF (black lines in fig. 10 and fig. 11) that both distortion parameters are initially decreasing at CCOP to rise again at CUOP. Similar phenomena have also been found by Brehm et al. (2014) for high Reynolds numbers of the incoming flow. The reason for this characteristic is the varying three dimensional shape of the flow separation and the segment based definition of the $DC60$ and $SC60$ distortion parameters (cf. Brehm et al. (2014)). For a lower Reynolds number level (SETF operation, dashed black lines), the shape of the separation changes in such a way that both $DC60$ and $SC60$ show continuously higher maxima with increased engine mass flow rate.

The situation for duct 2 is not as straight forward (blue and dashed blue lines): For ETF operation (blue lines) at CLOP, $SC60_{max}$ is almost equal and $DC60_{max}$ is even higher compared to SETF operation (dashed blue lines). However, the maxima of $DC60$ and $SC60$ are decreased significantly at CCOP analog to duct 1 in the ETF (blue lines), but much more pronounced. Increasing the engine mass flow rate up to operating point CUOP, the dependency on the mass flow rate for duct 2 in the SETF (dashed blue lines) is also equivalent to SETF operation of duct 1 (dashed black lines): The higher $\dot{m}_{red}$, the higher the strength of total pressure and swirl distortions become.

Not only the characteristic of the highly three dimensional recirculation structure originating from the upper intake lip (cf. fig. 5) which is varying with different Mach and Reynolds numbers, has an impact on the distortion patterns within the AIP. Also the influence of the spline-defined double s-shaped centerline and the strongly varying cross-sectional shapes (fig. 4) under different inflow conditions in terms of Mach and Reynolds number have to be taken into account.

Detailed evaluation of these phenomena is far beyond the scope of this paper but further research on the topics mentioned is planned in near the future.

Thus, the strength of both total pressure as well as swirl distortions for engine operating points featuring Mach number similarity in both facilities have to be determined individually for each duct geometry under consideration. Because of this, it must be concluded that a definition of a general "trade factor" for transfer of distortion parameters from the SETF to the ETF is not possible. Only for duct geometry 1, where a well defined separation region establishes, $DC60_{max}$ and $SC60_{max}$ are about 40% higher for operation in the SETF as a rule of thumb.

8. Conclusion and outlook

Within this paper, the transferability of aerodynamic results for two complex intake geometries operated in the Scaled Engine Test Facility (SETF) to operation in the full scale Engine Test Facility (ETF) has been investigated by means of CFD simulations. The main reason therefore is to combine the advantages of both test beds operated by the Institute of Jet Propulsion at the University of the German Federal Armed Forces Munich. The CFD setups have been validated with internally and externally available experimental data, respectively.

In order to ensure Mach number similar conditions concerning the duct inflow in both engine test facilities, a particular correlation procedure based on the reduced engine mass flow $\dot{m}_{red}$ has been established and validated.

The non-dimensional wall pressure distributions in both ducts operated in the ETF and the SETF are qualitatively similar. Quantitative deviations occur due to the immanent differences in the Reynolds number levels present and slightly different axial positions of the installation of duct geometry 2 (typical for unmanned military air systems).

Well-defined separation regions, as they are present in the single s-shaped duct geometry 1 (circular cross-sections), are more pronounced within the SETF due to the lower Reynolds number level. In turn also two introduced total pressure and swirl distortion parameters ($DC60$ / $SC60$) show maxima which are higher by about 40% for the SETF compared to the ETF.

Furthermore, fundamental differences in the dependency of $DC60$ and $SC60$ on the duct inflow Mach number in both facilities have been identified.

In case of duct 2, a highly three dimensional recirculation structure is developing around the intake lip. In addition to that, the mutual interdependencies of different inflow conditions in terms of Mach and Reynolds number and the double s-shaped centerline as well as the varying cross-sectional areas have to be taken into account. Therefore, an overall “trade factor" to transfer CFD results for distortion parameters from the SETF to full scale operation could not be established. From this, it must be concluded that each intake geometry to be operated in the ETF has to be compared individually.

Further activities on this topic will include the extension of the engine operating ranges which allow Mach number similar operations in both facilities. Furthermore, the use of URANS simulations and different turbulence models is considered to enhance CFD predictions of the region directly affected by the three dimensional recirculation structure around the intake lip of duct 2.

References

Berrier, B. L. & Allan, B. G., 2004, “Experimental and Computational Evaluation of Flush-Mounted S-Duct Inlets”, AIAA-2004-0764, 42nd AIAA Aerospace Sciences Meeting & Exhibit, 5-8 January 2004, Reno, Nevada, USA

Bindl, S., Muth, B. & Niehuis, R., 2009, “Experimental Investigations on Macro-Aerodynamics Within a Jet Engine Ground Test Facility”, AIAA-2009-4828, 45th AIAA Joint Propulsion Conference and Exhibit, 2-5 August 2009, Denver, CO, USA

Bindl, S., Muth, B., Stößel, M., Brehm, S. & Niehuis, R., 2012, “Experimental Investigation on the Ejector Pump Effect in Jet Engine Test Facilities”, Proceedings of the 4th International Symposium on Jet Propulsion and Power Engineering, September 10-12, 2012, Xi’an, China

Bindl, S., Muth, B., & Niehuis, R. 2013, “Adaptation of a Ground Test Facility to Operate a Modern Turbo-Jet Engine”, ISABE-2013-1307, Proceedings of the 21st International Symposium on Air Breathing Engines (ISABE), September 9-13, 2013, Busan, Korea

Bindl, S., Rademakers, R. P. M., Brehm, S. & Niehuis, R., 2015, “Aspects of Serpentine Inlets for Integrated Propulsion Systems”, ISABE-2015-22150, Proceedings of the 22nd International Symposium on Air Breathing Engines (ISABE), October 25-30, 2015, Phoenix, AZ, USA

Bissinger, N. C. & Breuer, T., 2010, “Basic Principles - Gas Turbine Compatibility - Intake Aerodynamic Aspects”, Encyclopedia of Aerospace Engineering, John Wiley & Sons Ltd.

Brehm, S., Kächele, T. & Niehuis, R., 2014, “CFD Investigations on the Influence of Varying Inflow Conditions on the Aerodynamics in an S-Shaped Inlet duct”, AIAA-2014-3595, 50th Joint Propulsion Conference and Exhibit, July 28-30, 2014, Cleveland, OH, USA

Cousins, W. T., 2004. “History, Philosophy, Physics and Future Directions of Aircraft Propulsion System/Inlet Integration”, ASME Turbo Expo 2004, Power for Land, Sea and Air, June 14-17, Vienna, Austria

Davis, M., Baker, W., Power, G. & Beale, D., 2002, “A Proposal for Integration of Wind Tunnel and Engine Test Programs for the Evaluation of Airframe-Propulsion Compatibility using Numerical Simulations”, Journal of Engineering for Gas Turbines and Power, 124, pp. 447-458.

Hamstra, J. W. & McCallum, B. N., 2010, “Tactical Aircraft Aerodynamic Integration”, Encyclopedia of Aerospace Engineering, John Wiley & Sons Ltd.

Kächele, T., Brehm, S. & Niehuis, R., “Parametric CFD Study on Performance of Double-S-Shaped Ducts with Varying Cross-Sectional Shapes”, In ISAIF12-037, Computational Aerothermodynamics of Internal Flows, July 13-16, 2015, Genova, Italy

Kächele, T., Brehm, S. & Niehuis, R., 2015, “Large Scale Numerical Parameter Study on Geometric Effects on Performance of Double-S-Shaped Ducts”, In ISABE-2015-22252, Proceedings of the 22nd International Symposium on Air Breathing Engines (ISABE), October 25-30, 2015, Phoenix, AZ, USA

Muth, B., Bindl, S., Stößel, M., Brehm, S. & Niehuis, R., 2012, “A CFD Study of the Ejector Pump Effect-within Jet Engine Test Facilities”, Proceedings of the 4th International Symposium on Jet Propulsion and Power Engineering, September 10-12, 2012, Xi’an, China

Rademakers, R., Bindl, S., Brehm, S., Muth, B. & Niehuis, R., 2013, “Investigation of Flow Distortion in an Integrated Inlet of a Jet Engine”, DLRK 301349, 62. Deutscher Luft- und Raumfahrtkongress 2013, 10.-12. September 2013, Stuttgart, Germany

Schmid, N. R., Leinos, D. C. & Fottner, L., 2000, “Steady Performance Measurements of a Turbofan Engine with Inlet Distortions Containing Co- and Counterrotating Swirl from an Intake Diffuser for Hypersonic Flight”, Journal of Turbomachinery, 123(2), pp. 379-385.

Sobester, A., 2007, “Tradeoffs in Jet Inlet Design: A Historical Perspective”, Journal of Aircraft, 44, pp. 705-717.

Vuillerme, A., Deck, S. & Chevrier, R., 2005, “Numerical Simulation of the Flow Inside an S-Shaped Intake Diffuser”, In European Conference for Aerospace Sciences (EUCASS)

Wellborn, S. R. & Okiishi, T. H., 1993, “A Study of the Compressible Flow through a Diffusing S-Duct”, NASA Technical Memorandum 106411